ISSN 1674-1056
http://cpb.iphy.ac.cn
http://iopscience.iop.org/cpb
中国物理 B
Chinese Physics
中国物理 Chinese Physics B

Effects of helium implantation on mechanical properties of $(Al_{0.31}Cr_{0.20}Fe_{0.14}Ni_{0.35})O$ high entropy oxide films

Zhao-Ming Yang(杨朝明), Kun Zhang(张坤), Nan Qiu(裘南), Hai-Bin Zhang(张海斌), Yuan Wang(汪渊), Jian Chen(陈坚)

Citation: Chin. Phys. B . 2019, 28(4): 046201. **doi:** 10.1088/1674-1056/28/4/046201
Journal homepage: http://cpb.iphy.ac.cn; http://iopscience.iop.org/cpb

What follows is a list of articles you may be interested in

First-principles investigations on structural stability, mechanical, and thermodynamic properties of LaT_2Al_{20} (T=Ti, V, Cr, Nb, and Ta) intermetallic cage compounds

Shanyu Quan(权善玉), Xudong Zhang(张旭东), Cong Liu(刘聪), Wei Jiang(姜伟)
Chin. Phys. B . 2018, 27(12): 126201. **doi:** 10.1088/1674-1056/27/12/126201

Effects of alloying element on stabilities, electronic structures, and mechanical properties of Pd-based superalloys

Pei Yan(闫佩), Xiao-Yu Chong(种晓宇), Ye-Hua Jiang(蒋业华), Jing Feng(冯晶)
Chin. Phys. B . 2017, 26(12): 126202. **doi:** 10.1088/1674-1056/26/12/126202

Investigation of mechanical properties of twin gold crystal nanowires under uniaxial load by molecular dynamics method

Guo-Wei Zhang(张国伟), Zai-Lin Yang(杨在林), Gang Luo(罗刚)
Chin. Phys. B . 2016, 25(8): 086203. **doi:** 10.1088/1674-1056/25/8/086203

First-principles calculation of the structural, electronic, elastic, and optical properties of sulfur-doping ε-GaSe crystal

Chang-Bao Huang(黄昌保), Hai-Xin Wu(吴海信), You-Bao Ni(倪友保), Zhen-You Wang(王振友), Ming Qi(戚鸣), Chun-Li Zhang(张春丽)
Chin. Phys. B . 2016, 25(8): 086201. **doi:** 10.1088/1674-1056/25/8/086201

Mechanical and thermodynamic properties of cubic YH_2 under high pressure：Prediction from first-principles study

Li Zhen-Li, Cheng Xin-Lu
Chin. Phys. B . 2014, 23(4): 046201. **doi:** 10.1088/1674-1056/23/4/046201

Effects of helium implantation on mechanical properties of $(Al_{0.31}Cr_{0.20}Fe_{0.14}Ni_{0.35})O$ high entropy oxide films*

Zhao-Ming Yang(杨朝明)[1,2], Kun Zhang(张坤)[1], Nan Qiu(裘南)[1], Hai-Bin Zhang(张海斌)[2], Yuan Wang(汪渊)[1,†], and Jian Chen(陈坚)[3,‡]

[1] *Key Laboratory of Radiation Physics and Technology of Ministry of Education, Institute of Nuclear Science and Technology, Sichuan University, Chengdu* 610064, *China*

[2] *Institute of Nuclear Physics and Chemistry, China Academy of Engineering Physics, Mianyang* 621900, *China*

[3] *Jiangsu Key Laboratory of Advanced Metallic Materials, School of Materials Science and Engineering, Southeast University, Nanjing* 211189, *China*

(Received 11 December 2018; revised manuscript received 3 February 2019; published online 19 March 2019)

It is widely accepted that helium (He) bubbles can prevent dislocations from moving and causing hardening and embrittlement of the material. However, He can affect the mechanical properties of materials in various ways. In this work, ultrafine nanocrystal high entropy oxide (HEO) films with He implantation are prepared by using a radio frequency (RF) reactive magnetron sputtering system to investigate the effects of He bubbles located at grain boundary on the mechanical properties of the films. The mechanical properties of the HEO films are investigated systematically via nanoindentation measurements. The results indicate that the grain boundary cavities induced by He implantation can degrade the hardness, the elastic modulus, and the creep resistance of the HEO films. The mechanical properties of the HEO films are sensitive to the interaction between the He bubbles and the dominating defects.

Keywords: helium accumulation, grain boundaries, mechanical properties, high-entropy oxides

PACS: 62.23.–c, 81.07.–b **DOI:** 10.1088/1674-1056/28/4/046201

1. Introduction

High entropy alloys (HEAs) have been rapidly developed as a promising functional and structural material due to their outstanding properties, such as high mechanical properties and excellent corrosion resistance.[1–3] In recent years, the concept of entropy stabilization for HEAs materials has also been extended to the composite oxides,[4] termed high entropy oxides (HEOs), which also exhibit remarkable performance including colossal dielectric constants,[5] excellent ionic conductivity,[6,7] and high temperature stability.[8,9] HEOs are even expected to be used as radiation tolerance materials or tritium permeation barriers in nuclear reactors, considering the outstanding radiation tolerance of high-entropy materials and the huge permeation reduction factor (PRF) of ceramic materials.[10–12]

In nuclear reactors, neutron bombardment can generate considerable concentration of He in the materials via nuclear reactions.[13] He atoms are insoluble in materials and thus segregate easily into He bubbles.[13–16] Many previous reports have shown that the He bubbles can suppress the dislocation gliding by pinning the dislocations to cause material to harden even at low concentration.[17,18] However, it should be noted that He bubbles can cause material to soften by increasing the free volume to facilitate the formation of the shear bands when they segregate into glassy phase.[19,20] He bubbles can also enhance the interface sliding by reducing the interfacial cohesive energy when they segregate along the interface between the multilayer films.[21] This indicates that He bubbles can have various effects on the mechanical properties of materials. So far, the mechanism of the He effects on the mechanical properties of the materials has not been fully elucidated by conventional dislocation pinning theory, which is mostly due to the complicated interaction between the He bubbles and the material defects, and, more importantly, the behavior of the material deformation strongly depends on the material defect type. For example, the grain boundary, rather than the dislocations, plays a decisive role in the plastic deformation of the ultrafine nanocrystal material whose grain diameter is less than 10 nm,[22] while the dislocation motion dominates the plastic deformation of the coarse crystal material because a lower energy is required by the grain boundary sliding and the grain boundary atom diffusion than by the dislocation proliferation.[23,24] Therefore, He bubbles should have deep effects on the mechanical properties of the ultrafine nanocrystal materials, which have been explored as alternative materials for nuclear reactors,[25] because He bubbles are favorable for being segregated at the grain boundaries when they

*Project supported by the National Natural Science Foundation of China (Grant Nos. 11775150 and 11505121).

†Corresponding author. E-mail: wyuan@scu.edu.cn

‡Corresponding author. E-mail: j.chen@seu.edu.cn

© 2019 Chinese Physical Society and IOP Publishing Ltd

are introduced.[26] However, we are still unable to accurately describe the effects of He bubbles at the grain boundary on the mechanical properties of the ultrafine nanocrystal materials, even though some theoretical and experimental efforts were devoted to understanding the effects of He on the mechanical properties of these materials.[27,28]

In this work, the (Al–Cr–Fe–Ni)O ultrafine nanocrystal HEO films with different He concentrations are prepared by a radio frequency (RF) reactive magnetron sputtering system under different He partial pressures. The ultrafine nanocrystals are easily formed in the HEO materials due to the sluggish diffusion effect of the elements in high entropy materials. The mechanical properties of the HEO films are systemically investigated by a nanoindentation test. Changes of the hardness, reduced elastic modulus and creep resistance of the ultrafine nanocrystal HEO films have been analyzed.

2. Materials and methods

(Al–Cr–Fe–Ni)O high-entropy oxide (HEO) films with He implantation were deposited on single crystal Si (100) substrates by an RF reactive magnetron sputtering system. Several circular aluminum, chromium, iron and nickel sectors (99.995% in purity and 1 mm in thickness) were combined into a sputtering target. The distance between the target and the substrate was maintained at 50 mm. The silicon substrates were cleaned ultrasonically with alcohol prior to being placed on the substrate holder. HEO films with He implantation were deposited in a stainless-steel vacuum chamber, and the basic pressure was 8.0×10^{-4} Pa prior to deposition. The target area was pre-sputtered for 20 min to remove impurities from the surface. A pure titanium (Ti) interlayer with a thickness of about 100 nm was deposited on the Si substrates prior to the deposition of HEO films. During the deposition of the HEO films with He implantation, pure Ar, O_2, and He were introduced into the chamber. The concentration of He introduced into the films was controlled by changing the partial pressure of He in a range of 0.1 Pa–0.3 Pa during deposition. The RF power was maintained at 100 W. With a similar procedure, the (Al–Cr–Fe–Ni)O HEO film was also deposited on the single crystal Si (100), which serves as a control sample. During the deposition of the (Al–Cr–Fe–Ni)O HEO film, pure Ar and O_2 were induced into the chamber. The rotation rate of the substrate holder was set to be 10 r/min to ensure elements uniformly distributed in the films, and the substrate was neither heated nor cooled intentionally during the deposition of the films. The thickness values of all of the films were kept at approximately 800 nm.

Rutherford backscattering spectrometry (RBS) was used to investigate the elemental compositions of the films with 2-MeV $^4He^+$ ions and at a backscattering angle of 160°. For a quantitative analysis of the elemental compositions of the films, the RBS spectra were fitted with simulation software RUMP 2.0. The evolution of the surface morphology of the film was investigated by an atomic force microscope (AFM, CSPM5500). Grazing-incidence (1°) x-ray diffraction (GIXRD, X'Pert Pro MPD DY129) measurements was performed to determine the crystal structure of the film by using a diffractometer with the Cu Kα radiation source operated at 40 kV and 35 mA. The microstructure of the as-deposited HEO film was further characterized by a high-resolution transmission electron microscope (HRTEM, Tecnai G2 F20S-TWIN).

A nanoindentation instrument (NanoTest Vantage) equipped with a Berkovich indenter was employed in ambient conditions to evaluate the mechanical properties of these films. The samples were cut into square slices each with a side length of 5 mm and stuck on the sample stand with cyanoacrylate adhesive prior to nanoindention tests. The adopted maximum load and the load rate were 6 mN and 0.5 mN/s during indenting, respectively. Peak loads were chosen such that the percentage of the penetration depths to the film thickness varied from 13%–15%, a range in which the substrate effect can be neglected.[29] Once the maximum load had been reached, the load was fixed and held for 50 s. In that process, the load-displacement and displacement-time curves were recorded simultaneously. The values of hardness and elastic module of the samples were derived from the load-displacement data according to the Oliver-Pharr method.[30] The displacement-dwell time curves can reflect the creep behavior of the films.[31] To avoid experimental error, each test was repeated 10 times.

3. Results and discussion

3.1. Elemental composition of film

The RBS spectra and the simulated results of the as-deposited and He-implanted films are shown in Fig. 1. The quantitative analysis shows that the as-deposited HEO film (Figure 1(a)) contains Al 15.5 at.%, Cr 10.0 at.%, Fe 7.0 at.%, Ni 17.5 at.% and O 50 at.%. Consequently, the stoichiometry of the as-deposited HEO film is referred to as $(Al_{0.31}Cr_{0.20}Fe_{0.14}Ni_{0.35})O$ film hereafter. For the He-implanted HEO films (Figs. 1(b)–1(d)), the calculated He concentrations of the HEO films with 0.1-Pa, 0.2-Pa, and 0.3-Pa He implantation are 9.5, 28.6, and 33.1 at.%, respectively, indicating that the He concentration increases with He partial pressure increasing during the film deposition.

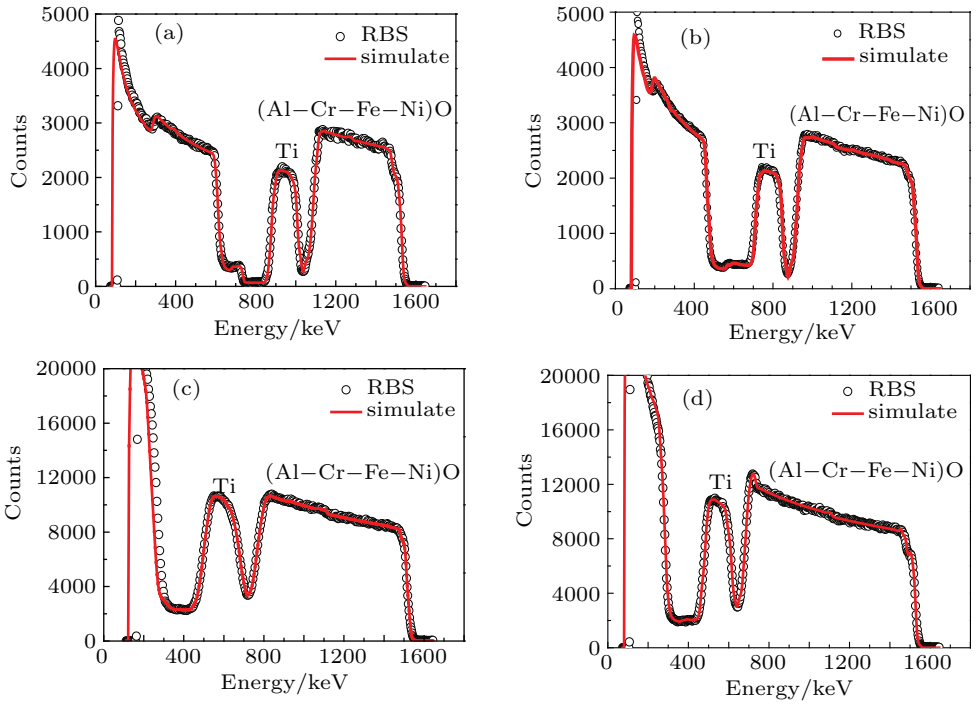


Fig. 1. RBS spectrum and simulated spectrum of (a) as-deposited (Al–Cr–Fe–Ni)O HEO film, (Al–Cr–Fe–Ni)O HEO films with (b) 0.1-Pa He, (c) 0.2-Pa He, and (d) 0.3-Pa He implantation.

3.2. Effects of He implantation on surface morphology and crystalline structure of HEO film

The evolutions of the surface morphology of the HEO films are shown in Fig. 2. The as-deposited HEO film (in Fig. 2(a)) has a flat and smooth surface with few sparsely distributed blisters. In contrast, a large number of blisters appear on the surfaces of the He-implanted films (in Figs. 2(b)–2(d)).

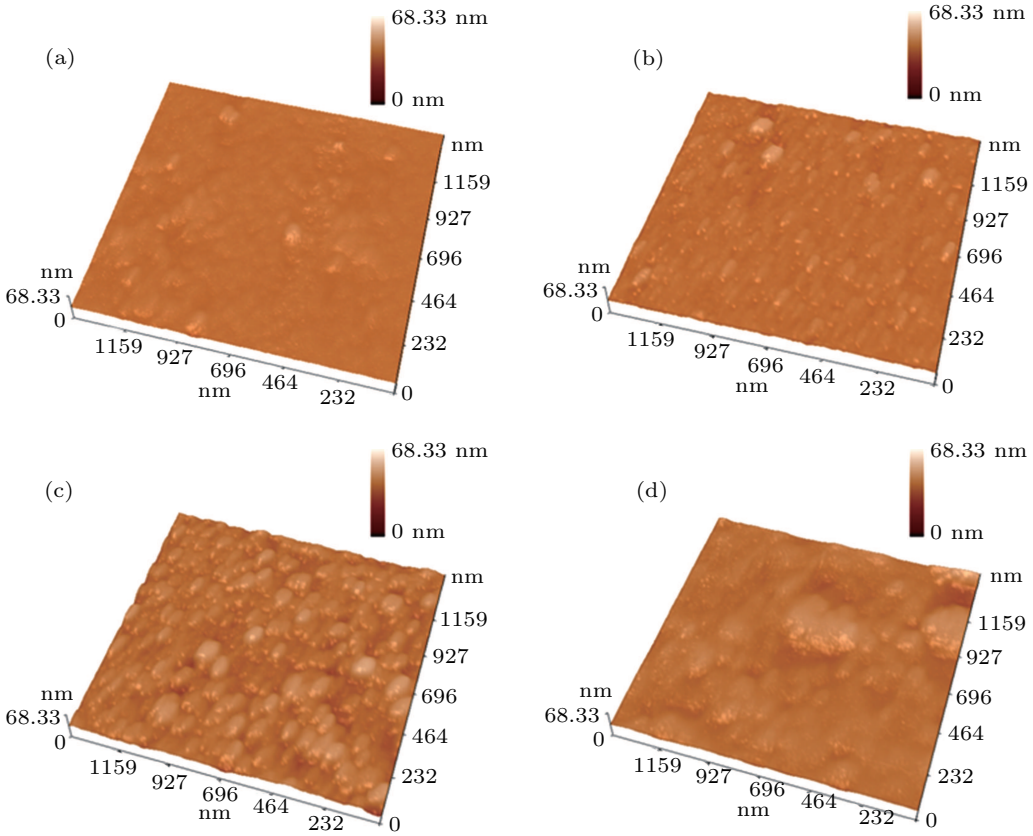


Fig. 2. Surface morphology of (a) the as-deposited HEO film, (b) HEO films with 0.1-Pa He, (c) 0.2-Pa He, and (d) 0.3-Pa He implantation.

It is also noted that with the increase of the implanted He content, the number of blisters decreases while the size of the blisters increases significantly. For the film with 0.3-Pa He implantation, the diameter of blisters can reach ~ 300 nm. This indicates that the implanted He can speed up small blisters coalescing and forming large blisters.

As described above, the surface morphology of the film is strongly related to the behaviors of the implanted He. Zheng *et al.*[32] pointed out that He can be introduced into the films by sputtering deposition and homogeneously. Cheng *et al.*[33] suggested that He bubbles can be formed in the Ti film once the atomic ratio of He/Ti exceeds 3.7 at.%. With the accumulation and growth of He bubbles at higher He concentration, surface blisters can be formed on the film surface.[34] In this work, the He concentration of the HEO films is greater than 9 at.%, which thus contributes to the formation of the He bubbles, and the change of the surface morphology with He implantation can be attributed to the aggregation and evolution of the He bubbles.

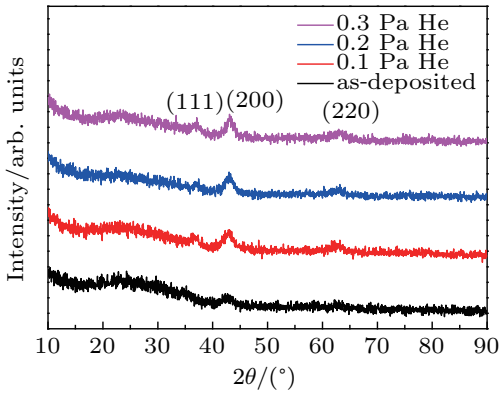


Fig. 3. GIXRD patterns of HEO films.

The GIXRD patterns of the HEO films are shown in Fig. 3. The results show that the He-implanted HEO films each have a typical face-centered-cubic (FCC) structure, Fm-$3m$ Rock-salt structure. The as-deposited HEO film shows only a single diffraction peak located at 42.6° in each of the GIXRD patterns. The HRTEM and the inset SAD images in Fig. 4(a) indicate that the as-deposited HEO film has the same crystalline structure as the He-implanted HEO film. The grain size of the as-deposited HEO film is about 3 nm–8 nm in diameter. Thus, it can be concluded that the as-deposited HEO film has the (200) preferential growth orientation along the x axis which is perpendicular to the single crystal Si (100) substrate. A large number of He bubbles (marked by white arrows in Fig. 4(b)) could be found in the HEO film with 0.3-Pa He implantation. It is also apparent from the HRTEM image of the HEO film with 0.3-Pa He implantation (Fig. 4(c)) that a large number of He bubbles (marked by red circles) with a diameter of about 1.5 nm–2 nm are mainly distributed at the grain boundary (the corresponding fast Fourier transform pattern is shown in Fig. 4(d)), while few He bubbles could be found inside the grains (the corresponding fast Fourier transform pattern is shown in Fig. 4(e)).

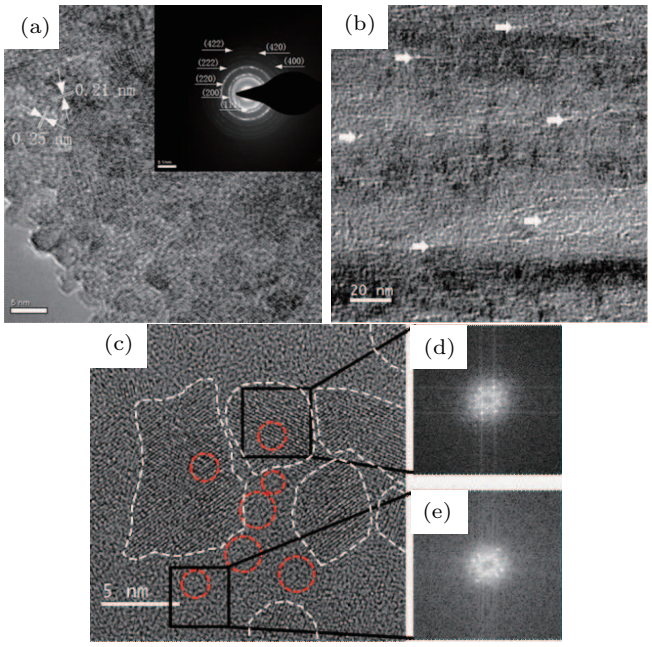


Fig. 4. HRTEM and SAED image (inset) of as-deposited HEO film, indicating that (a) film that has typical face-centered-cubic (FCC) structure, (b) low-magnification image that shows a large number of He bubbles (marked by white arrows) relatively evenly distributed in the HEO film with 0.3-Pa He implantation, (c) HRTEM image and (d)–(e) fast Fourier transform pattern of corresponding regions (marked by black rectangle in panel 4(c)). It is indicated that a large number of He bubbles (marked by red circles in panel 4(c)) with a diameter of about 1.5 nm–2 nm mainly distributed at the grain boundaries while few He bubbles existing inside grains (traced by white dash lines).

It is interesting to find that although the intensity of the (200) peak increases when He is introduced, two additional diffraction peaks of (111) and (220) located at 36.8° and 63.1° can also be found, respectively. These results show that the (200) preferential growth orientation of the HEO film is weakened when He is introduced. This can be attributed to the penning ionization which provides more ionized oxygen atoms to promote the formation of various textures when He atoms are introduced into the Ar–O_2 mixed atmosphere.[35] It should be mentioned that the (200) diffraction peak of the He-implanted HEO film shifts slightly to larger angle than that of the as-deposited HEO film. It indicates that the interplanar spacing of the HEO films decreases because of the He implantation. Moreover, the average grain size of the HEO film obtained from the GIXRD pattern (Fig. 3) ranges from 5.7 nm to 6.5 nm as listed in Table 1, suggesting that the change of the average grain size caused by the implanted He atoms can be neglected.

Table 1. Average grain sizes of the HEO films.

He partial pressure/Pa	0.1	0.1	0.2	0.3
Average grain size/nm	5.8	5.7	6.5	6.3

3.3. Effects of He implantation on mechanical properties of HEO films

The force-displacement curves of the HEO films measured by nanoindentation system are shown in Fig. 5. The indentation process includes the loading period with a load rate of 0.5 mN/s to the peak force 6 mN, the dwell period, at which the creeping motion of materials was recorded for 50 s, and finally the unloading period. The loading curves of the HEO films are smooth curves. The slopes of the unloading curves of the HEO films are similar. No evidence of "stair steps" typed discontinuity or excursion (also called pop-in) is found in any of the HEO films, indicating that there exists no staircase phenomenon in the indentation process. However, the loading curves of the HEO films significantly disperse, and the average slopes of loading curves of the HEO films gradually decrease with He concentration increasing. All of these results indicate that the indentation resistance of the HEO films is significantly changed by He implantation.

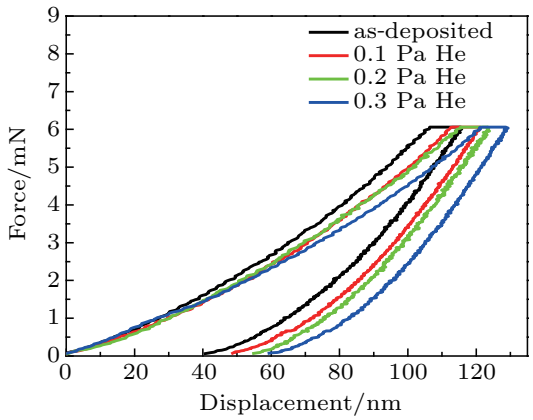


Fig. 5. Typical force-displacement curves of the HEO films.

The plots of average hardness (H) and reduced elastic modulus (E_r) of the HEO films *versus* He partial pressure are shown in Fig. 6. The as-deposited HEO film has the greatest H and E_r in all these films. Both H and E_r decrease with the increase of He concentration for the film. This result seems to contradict the often reported strengthening effects as the He bubbles can harden material by hindering the dislocations from moving.[17,18] However, since the synthesized HEO film consists of very small grains according to Table 1, the grain boundaries occupy a substantial fraction. Thus, the operating deformation mechanism in the ultrafine nanocrystals HEO film should be grain boundary accommodation rather than dislocation-mediated slip observed in common materials.[30–33]

Suzudo *et al.*[27] suggested that He bubbles can result in the formation of grain boundary cavities. The higher He content in the HEO film can expedite the formation of the grain boundary cavities. As the grain boundary cavities can disrupt the chemical bonds to form low-cohesive energy grain boundaries and reduce the resistant volume to mechanical stresses, the H and E_r continue to decrease with the as the size and density of the cavities increase.[14,36] The H and E_r deterioration caused by the grain boundary cavities can be described as flows:[37,38]

$$H = H_0 \exp(-bP), \tag{1}$$

$$E_r = E_{r0} \exp(-\beta P), \tag{2}$$

where H and E_r are the hardness and elastic modulus of the fully dense material, respectively, b and β are constant, P is the fraction of cavities.

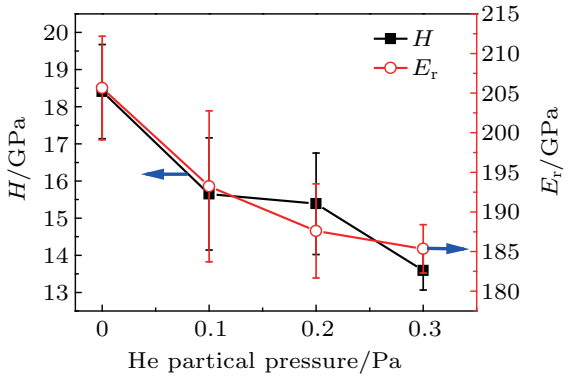


Fig. 6. Plot of hardness and reduced elastic modulus of HEO film versus He partial pressure.

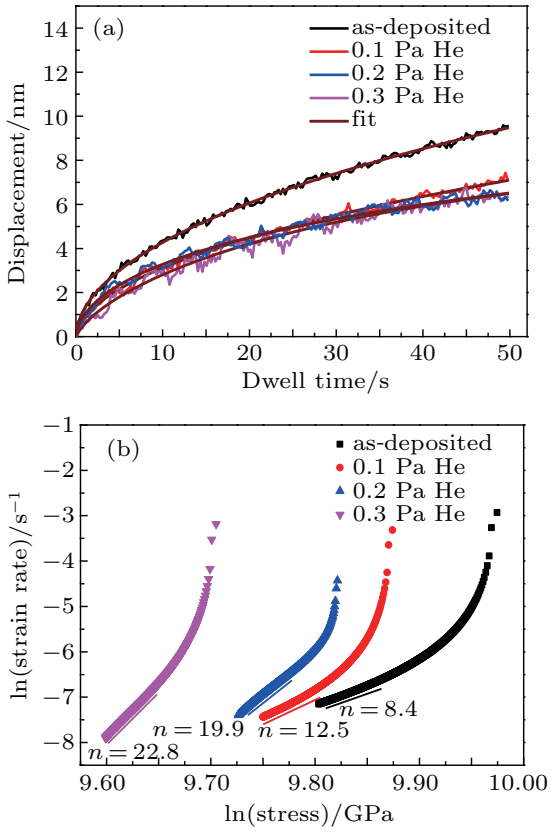


Fig. 7. (a) Normalized displacement-dwell time curves, and (b) ln(stain rate)–ln(stress) curves of HEO films.

Figure 7 shows the evolution of the creep behavior as a function of He partial pressure based on the experimental data of the HEO films. The normalized creep curves can be well

fitted, as shown in Fig. 7(a), by the following empirical fitting equation:[39]

$$h(t) = at^k + bt, \tag{3}$$

where $h(t)$ and t are the normalized displacement and the dwell time, respectively; a, b, and k are the fitting constants. When He atoms was introduced into the HEO films, the initial slope for each of the creep curves drops fleetly, as shown in Fig. 7(a). At the early stage, the as-deposited HEO film has the largest normalized displacement, while the He-implanted HEO film shows a similar displacement. As the holding time goes by, all the slopes gradually approach to steady states.

The diffusion creep, which is achieved mainly by Coble creep and Nabarro–Herring creep, is favorable for nanocrystal materials due to the fine grain size.[40] Atoms or vacancies can diffuse through the grains in Nabarro–Herring creep, while atoms or vacancies diffuse along grain boundaries in Coble creep. Coble creep is more likely to occur than Nabarro–Herring creep when the operate temperature is less than half the melting point ($0.5Tm$) as the activation energy required for Coble creep is less than that for Nabarro–Herring creep.[40] Therefore, Coble creep is the dominant mechanism for the ultrafine nanocrystal HEO films during nanoindentation creep at ambient temperature.

According to the general Norton relationship, the creep strain rate ($\dot{\varepsilon}$) is related to stress (σ), temperature (T), and microstructure by the following equation:[41]

$$\dot{\varepsilon} = \frac{A_1 D}{kT} \cdot \frac{\sigma^n}{d^m}, \tag{4}$$

where d is the grain size, m is the grain size exponent, and n is the stress exponent. The stress exponent (n) can reflect the creep mechanism of material in a certain environment in traditional creep testing.[31] According to Eq. (4), the stress exponent (n) can be obtained from the slope of the ln(strain rate)–ln(stress) curve in the part of steady-state creep:

$$n = \frac{\partial \ln(\dot{\varepsilon})}{\partial \ln(\sigma)}. \tag{5}$$

The ln(strain rate)–ln(stress) curves of the HEO films based on the fitting data of the creep curves and the derived n using Eq. (5) are shown in Fig. 7(b). The stress exponents are 8.4, 12.5, 19.9, and 22.8, corresponding to the film and the HEO films deposited with 0.1-Pa, 0.2-Pa, and 0.3-Pa He implantation, respectively. The obtained n by nanoindentation creep is higher than that by traditional creep tests. This is probably caused by the fact that the fully steady-state creep cannot be obtained for nanoindentation which is controlled by three-axis stress zone. With the increase of the creep depth, the continuously involved periphery is under the transition of creep behavior.[31] Although the derived n cannot reflect the real steady-state creep behavior, the increased tendency can be adopted to evaluate the different creep resistances among the different HEO films due to the similar loading conditions and material compositions. As given in Fig. 7(b), the value of n increases with He concentration increasing. It indicates that the creep resistance of the HEO film is deteriorated when the He concentration of the HEO film increases.

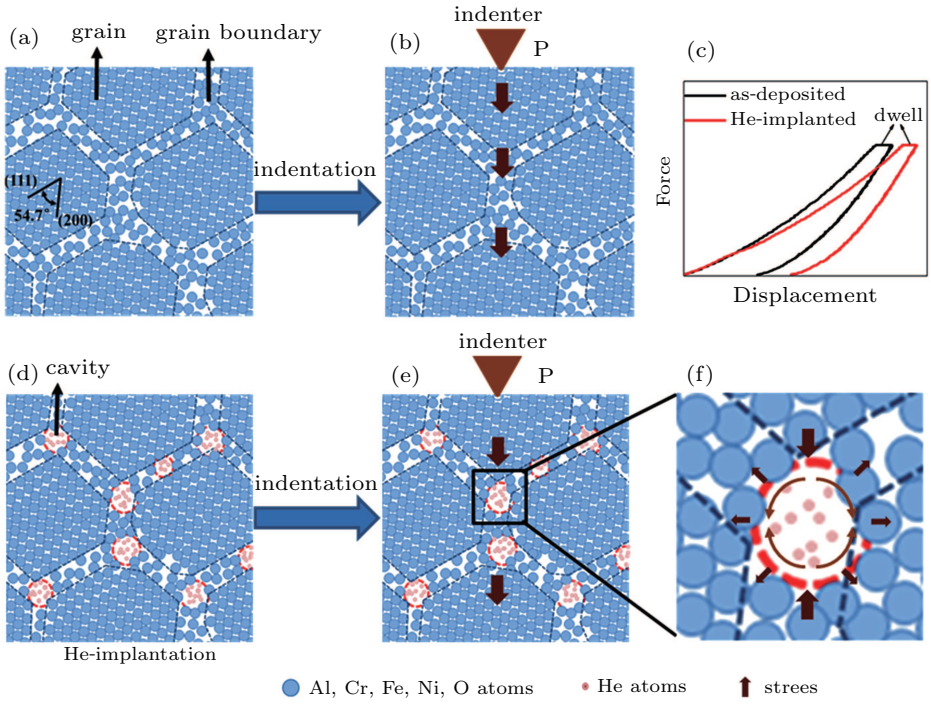


Fig. 8. Schematic illustration of the relationship between the grain boundary cavities induced by He implantation and the creep resistance of the HEO films: (a) the as-deposited HEO film, (b) indentation diagram of the as-deposited film, (c) force-displacement curve of films, (d) He-implanted film, (e) indentation diagram of He-implanted film, and (f) enlargement image of corresponding region in panel 8(e).

The effects of the grain boundary cavities induced by He implantation on the creep resistance of the HEO film are depicted schematically in Fig. 8. Hasselman *et al.*[41,42] suggested that the grain boundary cavities (in Fig. 8(d)) can enhance the local stress transfer to the adjacent region (in Fig. 8(f)), resulting in the increase of total strain and stress exponent. The enhanced creep by local stress transfer can be described as follows:[41]

$$\dot{\varepsilon} = \dot{\varepsilon}_0(1 + 4Na^3 n_c), \tag{6}$$

where $\dot{\varepsilon}_0$ is the creep rate of fully dense materials, N is the number of cavities in per unit area, a is the cavity radius, n_c is the additional stress exponent induced by the grain boundary cavities. Simultaneously, the grain boundary cavities can also speed up the diffusion of the atoms or vacancies by creating more internal surfaces (in Figs. 8(d)–8(f)) because the atom diffusion coefficient at surface is usually greater than that at grain boundary.[41] Therefore, the grain boundary cavities induced by He implantation can have considerable effects on the stress exponent of the HEO films, as shown in Fig. 8(c). It can be concluded that the mechanical properties of the HEO films with He implantation depend not only on the properties of the films themselves but also on the interaction between the He bubbles and the defects, which dominates the plastic deformation of material.

4. Conclusions

In this study, the $(Al_{0.31}Cr_{0.20}Fe_{0.14}Ni_{0.35})O$ HEO films with various He content are synthesized by magnetron sputtering. The microstructure analysis indicate that the (200) preferred orientation of the HEO films becomes weak when He is introduced into the films due to the higher ionization rate of oxygen in the deposition. The hardness, reduced elastic modulus and creep behavior for each of the HEO films are investigated with a nanoindentation system. It is found that the grain boundary cavities induced by He implantation can have a significant influence on the mechanical properties of the HEO films. The mechanical properties of the HEO films with He implantation depend not only on the properties of the films themselves but also on the interaction between the He bubbles and the defects that dominate the plastic deformation of the material.

References

[1] Huang P K, Yeh J W, Shun T T and Chen S K 2004 *Adv. Eng. Mater.* **6** 74

[2] Kumar N A P K, Li C, Leonard K J, Bei H and Zinkle S J 2016 *Acta Mater.* **113** 230

[3] Qiu X W, Zhang Y P, He L and Liu C G 2013 *J. Alloys Compd.* **549** 195

[4] Rost C M, Sachet E, Borman T, Moballegh A, Dickey E C, Hou D, Jones J L, Curtarolo S and Maria J P 2015 *Nat. Commun.* **6** 8485

[5] Berardan D, Meena A K, Franger S, Herrero C and Dragoe N 2017 *J. Alloys Compd.* **704** 693

[6] Sarkar A, Velasco L, Wang D, Wang Q, Talasila G, de Biasi L, Kubel C, Brezesinski T, Bhattacharya S S, Hahn H and Breitung B 2018 *Nat. Commun.* **9** 3400

[7] Qiu N, Chen H, Yang Z, Sun S, Wang Y and Cui Y 2019 *J. Alloys Compd.* **777** 767

[8] An, G, Wynn A P, Handley C M and Freeman C L 2018 *Acta Mater.* **146** 119

[9] Lin M I, Tsai M H, Shen W J and Yeh J W 2010 *Thin Solid Films* **518** 2732

[10] Lu C, Niu L, Chen N, Jin K, Yang T, Xiu P, Zhang Y, Gao F, Bei H, Shi S, He M R, Robertson I M, Weber W J and Wang L 2016 *Nat. Commun.* **7** 13564

[11] Sun S, Qiu N, Zhang K, He P, Ma Y, Gou F and Wang Y 2019 *Scr. Mater.* **161** 40

[12] Wang H, Ren F, Tang J, Qin W, Hu L, Dong L, Yang B, Cai G and Jiang C 2018 *Acta Mater.* **144** 691

[13] Tan L, Stoller R E, Field K G, Yang Y, Nam H, Morgan D, Wirth B D, Gussev M N and Busby J T 2016 *JOM* **68** 517

[14] Smith R W, Geng W T, Geller C B, Wu R and Freeman A J 2000 *Scr. Mater.* **43** 957

[15] Chen D, Tong Y, Li H, Wang J, Zhao Y L, Hu A and Kai J J 2018 *J. Nucl. Mater.* **501** 208

[16] Chen D, Tong Y, Wang J, Han B, Zhao Y L, He F and Kai J J 2018 *J. Nucl. Mater.* **510** 187

[17] Wei T, Zhu H, Ionescu M, Dayal P, Davis J, Carr D, Harrison R and Edwards L 2015 *J. Nucl. Mater.* **459** 284

[18] Hofmann F, Nguyen-Manh D, Gilbert M R, Beck C E, Eliason J K, Maznev A A, Liu W, Armstrong D E J, Nelson K A and Dudarev S L 2015 *Acta Mater.* **89** 352

[19] Chen X, Chen Y, Shi Y and Yang B 2018 *Ann. Nucl. Energy* **120** 835

[20] Li J, Wang Z L and Hufnagel T C 2002 *Phys. Rev. B* **65** 144201

[21] Callisti M, Karlik M and Polcar T 2016 *J. Nucl. Mater.* **473** 18

[22] Bartůněk V, Poryvai A and Ulbrich P 2017 *J. Fluorine Chem.* **200** 142

[23] Tjong S C and Chen H 2004 *Mater. Sci. Eng.: R: Rep.* **45** 1

[24] Chokshi C A 1993 *Mater. Sci. Eng. A* **166** 119

[25] Andrievskii R A 2010 *Phys. Met. & Metallogr.* **110** 229

[26] Wang X X, Niu L L and Wang S 2017 *J. Nucl. Mater.* **487** 158

[27] Suzudo T and Yamaguchi M 2015 *J. Nucl. Mater.* **465** 695

[28] Chen Z, Niu L L, Wang Z, Tian L, Kecskes L, Zhu K and Wei Q 2018 *Acta Mater.* **147** 100

[29] Saha R and Nix W D 2002 *Acta Mater.* **50** 23

[30] Pharr G M, Oliver W C and Brotzen F R 1992 *J. Mater. Res.* **7** 613

[31] Kaur N and Kaur D 2014 *Surf. Coat. Technol.* **260** 260

[32] Zheng H, Liu S, Yu H B, Wang L B, Liu C Z and Shi L Q 2005 *Mater. Lett.* **59** 1071

[33] Cheng G J, Shi L Q, Zhou X S, Liang J H, Wang W D, Long X G, Yang B F and Peng S M 2015 *J. Nucl. Mater.* **466** 615

[34] Lao Y, Niu W, Shi Y, Du H, Zhang H, Hu S and Wang Y 2018 *J. Alloys Compd.* **739** 401

[35] Patel K H and Rawal S K 2016 *Thin Solid Films* **620** 175

[36] Wei Q M, Li N, Mara N, Nastasi M and Misra A 2011 *Acta Mater.* **59** 6331

[37] Sanders P G, Eastman J A and Weertman J R 1997 *Acta Mater.* **45** 4019

[38] Paneto F J, Pereira J L, Lima J O, Jesus E J, Silva L A, Sousa Lima E, Cabral R F and Santos C 2015 *Int. J. Refract. Met. Hard Mater.* **48** 365

[39] Babu P S, Jha R, Guzman M, Sundararajan G and Agarwal A 2016 *Mater. Sci. Eng. A* **658** 415

[40] Norton F H 1936 *J. Am. Ceram. Soc.* **19** 129

[41] Fantozzi G, Chevalier J, Olagnon C and Chermant J L 2000 *Comprehensive Composite Materials* **31** 115

[42] Hasselman D P H and Venkateswaran A 1983 *J. Mater. Sci.* **18** 161